MDPI

Article

Research on Torque Performance of Marine Hybrid Excitation Synchronous Motors Based on PSO Optimization of Magnetic Permeability Structure

Qingliang Yang [1,2], Wendong Zhang [3] and Chaohui Zhao [3,*]

1   College of Mechanical Engineering, Shanghai Dianji University, Shanghai 201306, China; yangql@sdju.edu.cn
2   Logistics Engineering College, Shanghai Maritime University, Shanghai 201306, China
3   College of Electrical Engineering, Shanghai Dianji University, Shanghai 201306, China
*   Correspondence: zhaoch@sdju.edu.cn

Abstract: The rotor magnetic shunt structure hybrid excitation synchronous motor (RMS-HESM) has been widely used in marine propulsion due to its advantages of low loss and high efficiency. The objective of this paper is to improve the output torque capability of the hybrid excitation motor with a rotor magnetic shunt structure by conducting a multi-objective optimization design for the magnetic permeability structure. The first step involved establishing a mathematical analytical model of average torque and torque ripple based on the fundamental principle of motor magnetization. Next, the parameters of the magnetic permeability structure were designed and analyzed using the finite element simulation method. The impact of the variations in the parameters of the magnetic permeability structure on motor torque and no−load back electromotive force was examined. Additionally, a sensitivity analysis was performed on the design variables of the magnetic permeability structure, leading to the determination of optimization parameters based on the obtained results. The adaptive inertia weight-based particle swarm algorithm (PSO) was employed to conduct a multi-objective optimization design analysis. A comparative analysis on the average torque, torque ripple, and no−load back electromotive force of the motor before and after optimization was performed using the Maxwell and Workbench and Optislong joint simulation tools. This enhancement significantly improves the torque performance of the marine motor while simultaneously optimizing the no−load back electromotive force.

Keywords: hybrid excitation machine; particle swarm optimization; multi-objective optimization

1. Introduction

The motor, being an essential constituent of marine vessels, assumes a pivotal function in augmenting their operational efficiency [1–3]. The utilization of permanent magnet synchronous motors (PMSMs) is prevalent in maritime applications owing to their exceptional efficiency, power density, and reliability [4–6]. Nevertheless, when the ship is sailing in complex sea conditions, conventional PMSMs encounter challenges in flux adjustment. The sensitivity of permanent magnet materials to temperature necessitates careful consideration, as extreme temperatures can result in performance degradation or even permanent demagnetization. Additionally, the high-performance control system of PMSM is relatively intricate and requires advanced electronic control units and software, potentially increasing system complexity and cost. Consequently, additional design considerations are imperative to ensure motor reliability under all ship-operating conditions.

The hybrid excitation synchronous motor (HESM) integrates electrical excitation into the permanent magnet synchronous motor (PMSM), thereby retaining the inherent advantages of the PMSMs while enabling flux regulation [7–9]. By adjusting the external excitation current, it can modulate the strength of the magnetic field, ensuring high efficiency and performance across various operating conditions. Moreover, it offers a wide

range of speed regulations to cater to diverse application scenarios with distinct speed requirements. Additionally, its external excitation capability allows for supplementary magnetic field adjustment when necessary, thus enhancing motor reliability. Presently, marine hybrid excitation motors have garnered significant attention from both domestic and international researchers [10–15].

The literature [16] proposed a new type of hybrid excitation synchronous motor with a modular stator structure based on amorphous alloy material. Ref. [17] considers the characteristic differences and coupling effects between magnetic materials and proposes a preliminary design scheme for a composite permanent magnet motor to improve the utilization rate of permanent magnets and the superposition rate of torque components. The literature [18] investigates the impact of excitation current on the vibration and noise characteristics of a parallel hybrid excitation synchronous motor with rotor magnets. To improve the high torque density of the rotor magnetic shunt hybrid excitation motor, a study [19] investigated the impact of permanent magnet segmentation and modular rotor structure on reducing eddy current loss and temperature rise in the rotor. However, none of these studies have addressed the influence of the magnetic permeability structure on the torque characteristics of the RMS-HESM.

Currently, the scholars have discussed methods to improve the performance of synchronous motor electric drives, including advanced control algorithms and the internal structure of the motor. In Ref. [20], a sensor-less architecture based on the Extended Kalman Filter observer and on a feedback linearization control system is proposed. It is possible to assume a previously controlled solution, proposed by the authors, to reduce the intrinsic problem of the cogging torque. Ref. [21] examines the advantages of incorporating co-simulation and formal verification into a standard design flow for precision robotics applications of brushless electric drive systems. Additionally, Ref. [22] focuses on a design procedure for an advanced nonlinear control strategy that effectively mitigates the impact of torque oscillations, originating from various sources, on the precise positioning of the manipulator end-effector in synchronous electric drives. The literature [23] examines the effects of different rotor skew patterns on the cogging torque, the excitation torque ripple, the average torque, and the axial force in an interior permanent magnet synchronous motor. A genetic algorithm is used to minimize the cogging torque for different skew patterns based on analytical functions. The literature [24] focuses on a surface-mounted permanent magnet synchronous motor with a low cogging torque characteristic. Considering the interconnection of the stator segments, an equivalent modeling method of the segmented stator with assembly imperfection is introduced. A robust design process that incorporates a sensitivity analysis and a robust design optimization is proposed. Ref. [25] proposed a method to reduce the cogging torque by optimizing the size of the Halbach array's auxiliary pole. Ref. [26] studied a BLDC motor rated at 2.2 kW, 230 V, and 1450 rpm and used a unique combination of design techniques—changing the magnet edge embedding and changing the backlash angle to reduce the cogging torque. The literature [27,28] have, respectively, employed asymmetric V-shaped rotor structure, eccentric rotor, and stepped rotor to mitigate the cogging torque. In summary, advanced control algorithms and changing the internal structure of the motor each have their own pros and cons, which can be summarized as shown in Table 1.

Although these methods have yielded relatively favorable optimization results, the consideration of single variables in the optimization design often leads to unintended effects on the other electromagnetic characteristics of the motor. To further increase motor performance optimization, it is imperative to achieve higher output torque and lower torque ripple. Consequently, numerous scholars have applied multi-objective optimization algorithms to investigate motors. The literature [29] focused on a 100 kW ship-side thruster motor and addressed the issue of high harmonic content in the air gap magnetic flux density by implementing a rotor eccentricity design. Building upon this, the hybrid Taguchi method of genetic algorithm was employed to optimize the structural parameters of the rotor, resulting in improved motor efficiency and reduced costs. Compared to single-

objective optimization designs, the multi-objective optimization algorithms offer improved overall motor performance optimization capabilities, simplifying and enhancing efficiency in optimizing complex-structured motors [30,31].

Table 1. Pros and cons of both approaches.

Method	Pros	Cons
Advanced Control Algorithms	1. Improves the dynamic response and precision of the motor.	1. Control systems are complex, requiring higher-level programming and debugging.
	2. Performance improvements can be made via software updates without physical changes to the motor.	2. High computational power is required for the controller.
	3. Enables more functionality and operational modes, increasing motor adaptability.	3. Advanced algorithms may require additional sensors or hardware resources.
	4. Optimizes motor performance under various operating conditions, improving efficiency.	4. Development may be costly and require specialized knowledge.
The Optimization of Motor Internal Structure	1. Improved design reduces losses and increases efficiency.	1. Optimized designs may lead to increased manufacturing costs.
	2. Directly affects the physical characteristics of the motor, such as reducing noise and vibration.	2. Structural changes may impact the size and weight of the motor.
	3. Improved stability and reliability during long-term operation.	3. Physical modifications may be impractical or too costly for existing motors.
	4. Once implemented, no further adjustments or maintenance are required.	4. Design flaws could require a redesign and remanufacturing, affecting time to market.

The focus of this study is on the RMS-HESM as the research subject, and it utilizes Maxwell and Workbench and Optislong joint simulation tools to optimize the length, thickness, and auxiliary slots of the motor's magnetic permeability structure. The optimization objectives include the average torque, torque ripple, and no−load back electromotive force. Sensitivity analysis is conducted to determine the influence of different input parameters on these performance metrics. The particle swarm algorithm based on adaptive inertia weight is employed for the multi-objective optimization design analysis to obtain optimal design variables.

The novelty and contribution of this paper lie in proposing an optimal design scheme for the pole claws of the RMS-HESM. This optimization scheme can be applied to the same type of RMS-HESM, combining sensitivity analysis and adaptive inertia weighting. Integrating with the particle swarm algorithm effectively simplifies the design process, reduces three-dimensional finite element calculations, and significantly enhances the torque output and flux adjustment capabilities in marine motor applications.

The paper is structured as follows: Section 2 provides an introduction to the topology and working principle. Section 3 analyzes the impact of the magnetic permeability structure parameters on the motor torque characteristics. Section 4 examines the sensitivity of the optimization parameters for the permeability structure and conducts a multi-objective optimization analysis, comparing the electromagnetic performance between the initial and optimized designs. Finally, in Section 5, a summary of this paper is presented.

2. Theoretical Analysis of Motor Structure and Torque

2.1. Structural Parameters of RMS-HESM

The RMS-HESM utilizes a magnetic shunt structure to regulate the magnetic flux field through the adjustment of the excitation current flux. Figure 1 illustrates its primary configuration, while Table 2 presents its key parameters. The motor consists of the stator core, rotor core, permanent magnet, armature winding, N-pole magnetic bridge, S-pole magnetic bridge, DC excitation winding, and annular magnetic bridge as its main components. By

manipulating the current in the DC excitation winding, both magnetization and demagnetization effects can be achieved. The N-pole magnetic bridge, S-pole magnetic bridge, and annular magnetic bridge collectively form what is referred to as the "magnetic structure".
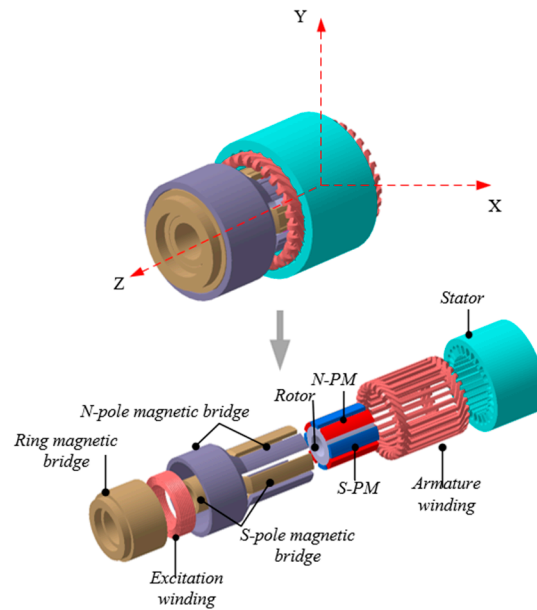

Figure 1. Schematic diagram of RMS-HESM structure.

Table 2. Main Parameters Of RSM-HESM.

Parameter	Numerical Value
Slots(Z_s)/Pole pairs(p)	27/4
Stator outer diameter/(mm)	122
Stator inner diameter/(mm)	77
Stator core length/(mm)	70
Ring magnetic bridge length	50
Pole claw pitch distance	20
Pole claw thickness	6
Permanent magnet thickness	5.75
DC excitation winding turns/Nc	600

Among them, the N-pole magnetic bridge, the S-pole magnetic bridge, and the annular magnetic bridge are collectively called the magnetic structure. The cross-sectional view is shown in Figure 2. The main structural parameters are shown in Table 3. L_1 is the width of the magnetic bridge. L_2 is the pole claw slope shoulder distance, C_{thick} is the thickness of the magnetic bridge, and P_{thick} is the thickness of the permanent magnet.

Table 3. Main Parameters Of magnetic structure.

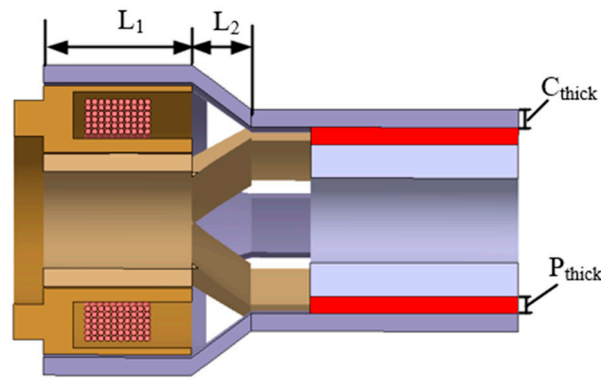| Parameter	Numerical Value
L_1/(mm)	50
L_2/(mm)	20
C_{thick}/(mm)	6
P_{thick}/(mm)	5.75

Figure 2. Magnetic structure cross-sectional view.

2.2. Working Principles of RMS-HESM

The RMS-HESM is equipped with two sources of magnetic potential: one being the permanent magnet, which generates both radial and axial magnetic flux (as shown by the solid and dotted lines in Figure 3), and the other being the DC field winding. By adjusting the magnitude and direction of the excitation winding current, it is possible to alter the resulting magnetic flux in the air gap.
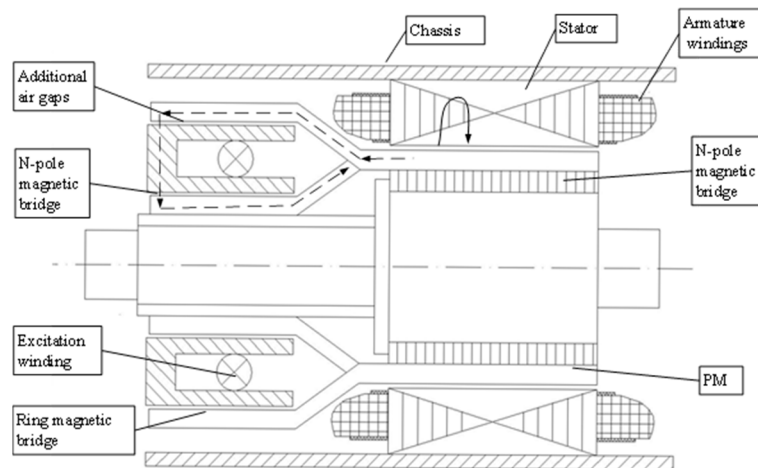

Figure 3. Flux path of RMS-HESM.

The radial magnetic flux path consists of the following components: N-pole magnet → main air gap δ_N → stator teeth and yoke → main air gap δ_S → S-pole magnet → rotor core → N-pole magnet.

The axial magnetic flux path includes N-pole magnet → N-pole magnetic bridge → additional air gap δ_{11} → ring magnetic bridge → additional air gap δ_{12} → S-pole magnetic bridge → S-pole magnet → rotor core → N-pole magnet.

The energization of the field winding results in a reduction in the axial shunt magnetic flux Φ_{AX}, while simultaneously increasing the radial flux path. The motor's equivalent circuit is depicted in Figure 4a. Under ideal conditions, $R_{\delta N} = R_{\delta S} = R_\delta$; $R_{PMN} = R_{PMS} = R_{PM}$; $F_{PMN} + F_{PMS} = F_{PM}$; $R_{\delta 11} + R_{\delta 12} = R_{\delta 1}$, thus simplifying the motor's equivalent circuit as shown in Figure 4b. δ_N is the N-pole air gap magnetic resistance; $R_{\delta S}$ is the S-pole air gap magnetic resistance; R_A is the armature tooth and yoke magnetic resistance in series with the main air gap; R_{PMN} is the magnetic resistance of the N-pole permanent magnet; R_{PMS} is the S-pole permanent magnet. The magnetic resistance of the additional air gap between the magnetic bridge and the annular magnetic bridge; R_{FE} is the magnetic resistance of the axial magnetic circuit; F_{EM} is the excitation flux provided by the excitation winding. Φ_{AX} is the magnetic flux passing through the magnetic circuit. The influence of the permanent magnet and permeable bridge thickness on the magnetic circuit's permanent

magnet reluctance R_{PM}, the permanent magnet magnetic potential F_{PM}, and the axial magnetic circuit reluctance R_{FE} can be observed in Figure 4b.
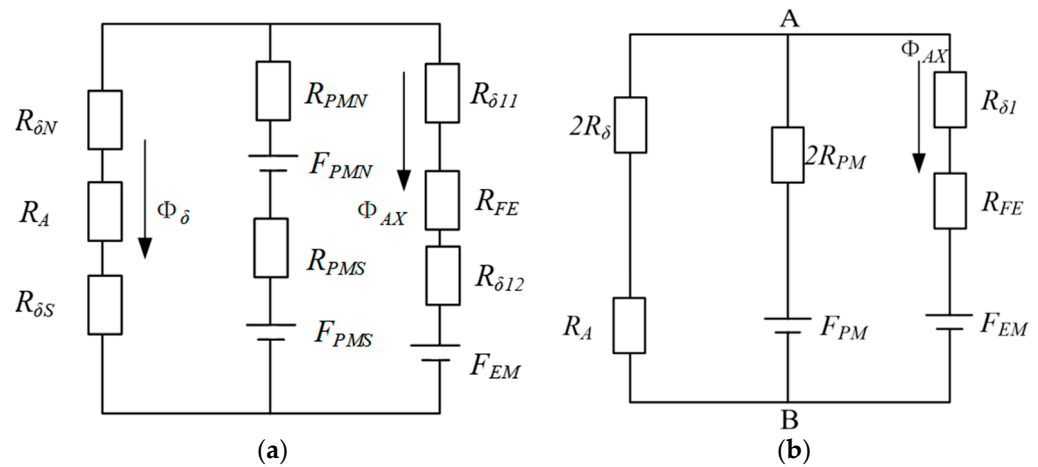
Figure 4. Equivalent magnetic circuit diagram of the motor at the magnetic shunt point. (**a**) Equivalent magnetic circuit of HESM; (**b**) Simplified magnetic circuit of HESM.

The presence of a magnetic shunt allows the magnetic flux generated by the permanent magnet to not only form a radial magnetic circuit through the main air gaps $R_{\delta N}$, $R_{\delta S}$, and R_A but also establish an axial magnetic circuit through the extension of the magnetizer and additional air gaps.

2.2.1. The Main Air Gap Flux of the Motor When the Excitation Current Is Zero ($I_f = 0$)

The excitation magnetic potential is non-existent when there is no excitation current in the excitation winding, The expression of the air gap main magnetic flux $\Phi_{\delta 1}$ can be obtained from the equivalent magnetic circuit:

$$\Phi_{\delta 1} = \Phi_{PM} - \Phi_{AX} \tag{1}$$

$$F_{PM} = \Phi_{PM} \cdot R_{PM} \tag{2}$$

$$R_{PM} = \frac{C_{thick}}{\mu_{Fe} s_{Fe}} + \frac{P_{thick}}{\mu_{PM} s_{PM}} \tag{3}$$

$$R_{AX} = \frac{L_1 + L_2}{\mu_{Fe} s_{Fe}} \tag{4}$$

where F_{PM} is the magnetomotive force of the permanent magnet. The Equations (1)~(4) can be combined to derive Equation (5):

$$\Phi_{\delta 1} = \frac{F_{PM}}{\frac{C_{thick}}{\mu_{Fe} s_{Fe}} + \frac{P_{thick}}{\mu_{PM} s_{PM}}} - \frac{F_{PM}}{\frac{L_1 + L_2}{\mu_{Fe} s_{Fe}}} \tag{5}$$

The implication of Equation (5) is evident. When C_{thick} and P_{thick} remain unchanged, consider changing L_1 and L_2 greater than 0. ($C_{thick}/\mu_{Fe} s_{Fe} + P_{thick}/\mu_{PM} s_{PM}$) is considered an immutable truth, $\lambda_1 > 0$. The F_{PM} is considered a constant C_1, which is greater than 0. The $\mu_{Fe} s_{Fe}$ is considered a constant λ_{Fe}, which is greater than 0. The Equation (6) is reached as follows:

$$\Phi_{\delta 1} = \frac{C_1}{\lambda_1} - \frac{C_1}{\frac{L_1 + L_2}{\lambda_{Fe}}} = \frac{C_1}{\lambda_1} - \frac{C_1 \lambda_{Fe}}{L_1 + L_2} \tag{6}$$

The C_1/λ_1 is considered a constant C, which is greater than 0. The $C_1\lambda_{Fe}$ is considered a constant Z, which is greater than 0. The Equation (6) can be combined to derive Equation (7):

$$\Phi_{\delta 1} == \frac{C_1}{\lambda_1} - \frac{C_1\lambda_{Fe}}{L_1 + L_2} = C - \frac{\frac{Z}{L_2}}{\frac{L_1}{L_2} + 1} \tag{7}$$

Equation (7) reveals that the magnitude of the main air gap magnetic flux is intricately linked to both the width of the magnetic bridge (L_1) and the distance between pole claw sloping shoulders (L_2). Specifically, when L_1 remains constant, reducing L_2 will result in a decrease in the main magnetic flux $\Phi_{\delta 1}$; the smaller the length of L_2, the greater the ratio of L_1/L_2 and the larger the value of $\Phi_{\delta 1}$. When L_2 remains unchanged, a decrease in L_1 will result in a reduction in the L_1/L_2 ratio, consequently leading to a decrease in the main magnetic flux $\Phi_{\delta 1}$ of the motor.

2.2.2. The Main Air Gap Flux of the Motor When the Excitation Current Is Not Equal to Zero ($I_f \neq 0$)

When the excitation current flows into the excitation winding, if the excitation magnetic potential can completely offset the permanent magnet magnetic potential in the axial magnetic shunt, then $\Phi_{AX} = 0$. All the permanent magnet flux passes through the main air gap. At this time, the main air gap flux is $\Phi_{\delta 1}$, where $\mu_{PM}S_{PM} = \lambda_{PM}$ can be obtained from the Formulas (8) and (9):

$$\Phi_{\delta 2} = \Phi_{PM} = \frac{F_{PM}}{R_m} = \frac{\lambda_1}{\frac{C_{thick}}{\lambda_{Fe}} + \frac{P_{thick}}{\lambda_{PM}}} = \frac{\lambda_1\lambda_{Fe}\lambda_{PM}}{C_{thick}\lambda_{PM} + P_{thick}\lambda_{Fe}} = \frac{\frac{\lambda_1\lambda_{PM}}{P_{thick}}}{\frac{C_{thick}\lambda_{PM}}{P_{thick}\lambda_{Fe}} + 1} \tag{8}$$

$$\Phi_{\delta 2} = \Phi_{PM} = \frac{F_{PM}}{R_m} == \frac{\lambda_1}{\frac{C_{thick}}{\lambda_{Fe}} + \frac{P_{thick}}{\lambda_{PM}}} = \frac{\lambda_1\lambda_{Fe}\lambda_{PM}}{C_{thick}\lambda_{PM} + P_{thick}\lambda_{Fe}} = \frac{\frac{\lambda_1\lambda_{Fe}}{C_{thick}}}{1 + \frac{P_{thick}\lambda_{Fe}}{C_{thick}\lambda_{PM}}} \tag{9}$$

When considering that P_{thick} is constant, $\lambda_1\lambda_{PM}$ is regarded as a fixed value constant, and $\lambda_{PM}\lambda_{Fe}$ is a fixed value, and Equation (10) can be obtained from Equation (8):

$$\Phi_{\delta 2} = \frac{\frac{\lambda_1\lambda_{PM}}{P_{thick}}}{\frac{C_{thick}\lambda_{PM}}{P_{thick}\lambda_{Fe}} + 1} \approx \frac{1}{C_{thick}} \tag{10}$$

When considering that C_{thick} is constant, $\lambda_1\lambda_{Fe}$ is regarded as a fixed value constant, and $\lambda_{PM}\lambda_{Fe}$ is a fixed value, and Equation (11) can be obtained from Equation (9):

$$\Phi_{\delta 2} = \frac{\frac{\lambda_1\lambda_{Fe}}{C_{thick}}}{1 + \frac{P_{thick}\lambda_{Fe}}{C_{thick}\lambda_{PM}}} \approx \frac{1}{P_{thick}} \tag{11}$$

Equations (10) and (11) reveal that when $I_f \neq 0$, the excitation magnetic potential can effectively counterbalance the permanent magnet magnetic potential in the axial magnetic shunt. Consequently, the magnitude of the main air gap flux is closely associated with C_{thick} and P_{thick}: increasing C_{thick} or P_{thick} will result in a reduction in the main magnetic flux $\Phi_{\delta 2}$; thus, thicker values for C_{thick} and P_{thick} correspond to smaller $\Phi_{\delta 2}$, whereas thinner values lead to larger $\Phi_{\delta 2}$.

The basic electromagnetic torque expression of the motor:

$$T = K\Phi I \tag{12}$$

where T is the torque, k is the proportionality constant, Φ is the magnetic flux, and I is the current. The change in torque primarily relies on Φ under the condition of maintaining the rated load, with I remaining unchanged. When $I_f = 0$, C_{thick} and P_{thick} remain unchanged. Consider changing L_1 and L_2. When L_1 remains constant, reducing the L_2 will result in a

decrease in torque; as L_2 becomes shorter, the ratio of L_1 to L_2 increases, indicating a larger electromagnetic torque of the motor. Conversely, if L_2 is longer, the electromagnetic torque of the motor will be smaller. When L_2 remains unchanged, the smaller the value of L_1, the lower the ratio of L_1 to L_2 and consequently, the reduced electromagnetic torque of the motor. When considering $I_f \neq 0$, it is important to note that by taking into account complete offsetting between excitation magnetic potential and permanent magnet magnetic potential in axial magnetic shunt, torque becomes solely dependent on C_{thick} and P_{thick}. Increasing the thicknesses of C_{thick} and P_{thick} results in decreased torque, while conversely, greater torque is achieved with thinner values.

It can be seen from Equation (12) that the average torque of the motor output is related to the air gap magnetic permeability and the stator and rotor magnetomotive force. The main air gap flux is closely associated with the magnetic structure of the pole claw, which includes L_1, L_2, C_{thick}, and P_{thick}. This can be observed by deriving formulas (7), (10), and (11). The main air gap flux can be further changed by changing the magnetic structure, thereby affecting the torque characteristics of the motor. In order to further verify the analysis, the finite element simulation method is used for further verification.

3. The Influence of Structural Parameters of Magnetic Permeability on the Characteristics of Motor Torque

In order to verify the correctness of the analytical analysis in the previous chapter, this chapter compares and analyzes the average output torque, torque ripple, and no−load back potential under the combination of the three groups of the structural parameters by finite element simulation method, and discusses the optimization effect of a single group of parameters on the optimization target, which lays a foundation for the next chapter of multi-objective optimization.

3.1. The Influence of Permanent Magnet and Pole Claw Thickness on Average Torque, Torque Ripple, and No−Load Back Electromotive Force

The N and S poles of the permanent magnet in the RMS-HESM are positioned to overlap with their respective magnetic bridge pole claws. The operating point of the permanent magnet is influenced by changes in its thickness along the magnetizing direction, while the path of electric excitation flux is affected by the thickness of the magnetic pole claws. The thickness ratio of the permanent magnets and magnetic pole claws needs to be reasonably designed without altering the fundamental structure of the motor. Finite element simulation analysis was conducted on the motor under both rated load and no−load conditions. The motor operating conditions are shown in Table 4.

Table 4. Motor operating condition.

| Parameter	Numerical Value
Power/(kW)	4
Rated speed(r/min)	1500
Rated torque/(N·m)	6
DC excitation current range/(A)	[−3, 3]

Set the pole claw thickness C_{thick} to vary from 6 mm to 8 mm in steps of 1 mm, and the permanent magnet thickness P_{thick} to vary from 6 mm to 8 mm in steps of 0.5 mm. The optimization results of P_{thick} and C_{thick} changes are shown in Table 5. The average torque and torque ripple changes in the motor are obtained, as shown in Figure 5. As the thickness of the pole claw gradually increases, the average torque of the motor decreases. When the thickness of both poles is 6 mm, the average torque value reaches the maximum of 6.37 N·m. When the thickness of the pole claw is 6 mm, the torque ripple first increases and then decreases as the thickness of the permanent magnet increases, reaching 4.23% when the thickness of the permanent magnet is 6 mm. The noteworthy observation is that when the pole claw thickness is 7 mm and the permanent magnet thickness is

8 mm, the torque ripple reaches a minimum value of 3.44%, albeit with a relatively low average torque of only 5.85 N·m. To conclude, the impact of combining the pole claws and varying permanent magnet thickness on both the average torque and torque ripple does not exhibit a linear relationship. Hence, it becomes imperative to maximize the average torque while minimizing the torque ripple, all while optimizing the utilization of the permanent magnets. The comparison of the amplitude changes in the no−load back electromotive force under different thickness combinations at the rated speed of the motor is illustrated in Figure 6. As C_{thick} increases, there is a general decrease in the amplitude of the no−load back electromotive force, reaching its maximum value when C_{thick} is 6 mm and P_{thick} is 6.5 mm, which amounts to 537.57 V. It can be observed from Figure 4 that with a constant thickness of the permanent magnet, as C_{thick} gradually increases, there is a decrease in both the average torque and torque ripple of the motor. This phenomenon can be attributed to an unchanged thickness of the permanent magnet and an increased thickness of the pole claws in the magnetic bridge. Consequently, there is an increase in magnetic flux shunted from the permanent magnet to the pole claws, leading to a weakening of the magnetic flux Φ_δ entering the main air gap. These observations align with the analytical formulas (10) and (12).

Table 5. The optimization results of P_{thick} and C_{thick} changes.

C_{thick} / P_{thick}		6 mm	6.5 mm	7 mm	7.5 mm	8 mm
6 mm	Torque/(N·m)	6.3784	6.3451	6.3245	6.2059	6.1206
	Torque ripple/(%)	4.2366	4.7355	4.6754	4.5824	4.6339
	EMF/(V)	396	537.6	405.4	447.9	393.7
7 mm	Torque/(N·m)	5.8855	5.8906	5.8743	5.8769	5.8547
	Torque ripple/(%)	4.6548	4.4312	4.5324	4.5261	3.4408
	EMF/(V)	412.5	387.5	376.5	425.6	432.4
8 mm	Torque/(N·m)	5.5993	5.6387	5.7047	5.6187	5.6223
	Torque ripple/(%)	4.5970	4.7643	3.7666	4.7837	4.6359
	EMF/(V)	387.4	423.5	461.4	404.5	377.2
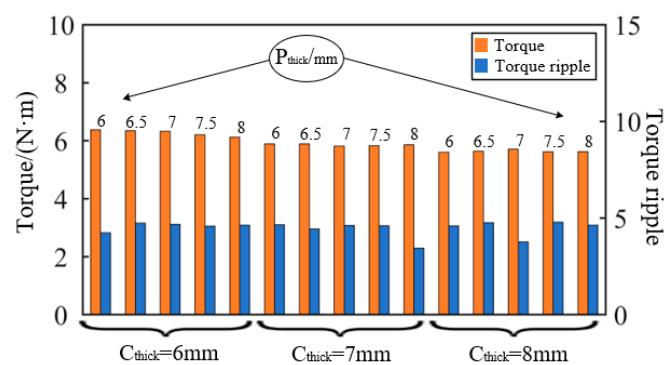
Figure 5. Analysis of the impact of the thickness ratio of the permanent magnets and pole claws on the average torque and torque ripple.
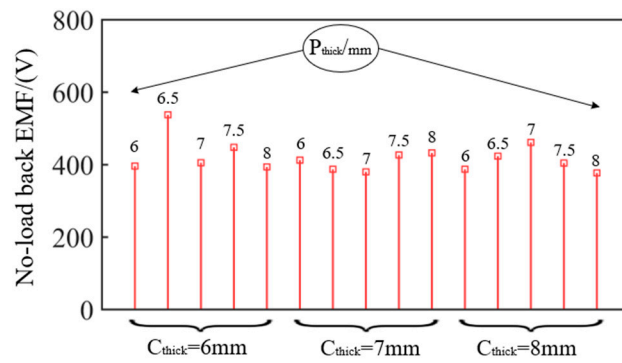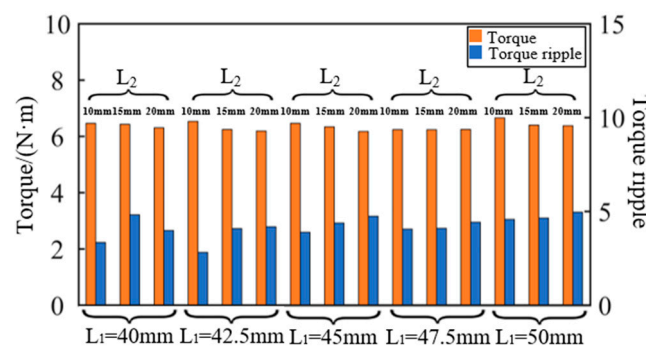
Figure 6. Analysis of the influence of the thickness ratio of the permanent magnets and pole claws on the amplitude of the no−load back electromotive force.

3.2. The Influence of the Sloping Shoulder Distance of the Pole Claws and the Length of the Annular Magnetic Bridge on the Average Torque, Torque Ripple, and No−Load Back Electromotive Force

In order to further advance the power density of the CC, while reducing its size and weight, parametric design was conducted on the pole claw sloping shoulder distance and thickness parameters of the annular magnetic bridge, followed by finite element analysis for simulation purposes. The design range of the pole claw sloping shoulder distance is 10–20 mm, with a step length of 2.5 mm, and the length of the annular magnetic bridge is varied within a range of 40–50 mm, with a step length of 2.5 mm. The optimization results of L_1 and L_2 changes are shown in Table 6. The average value of the obtained torque and the changes in the torque ripple are illustrated in Figure 7. The peak-to-peak value of the no−load back electromotive force is depicted in Figure 8.

Table 6. The optimization results of L_1 and L_2 changes.

L_2	L_1	40 mm	42.5 mm	45 mm	47.5 mm	50 mm
10 mm	Torque/(N·m)	6.4642	6.5343	6.4633	6.238	6.6591
	Torque ripple	3.3509	2.8165	3.9223	4.06	4.58
	EMF/(V)	392.27	383.12	373.54	377.41	393.78
15 mm	Torque/(N·m)	6.4306	6.2450	6.3416	6.2367	6.4
	Torque ripple	4.8173	4.0841	4.3863	4.10	4.65
	EMF/(V)	440.96	422.76	373.98	375.55	407.26
20 mm	Torque/(N·m)	6.3038	6.1929	6.1744	6.2325	6.38
	Torque ripple	3.9811	4.1873	4.75	4.4654	4.96
	EMF/(V)	382.32	384.01	376.48	376.67	422.24

Figure 7. Analysis of the influence of the pole claw sloping shoulder distance and annular magnetic bridge length on the average torque and torque ripple.
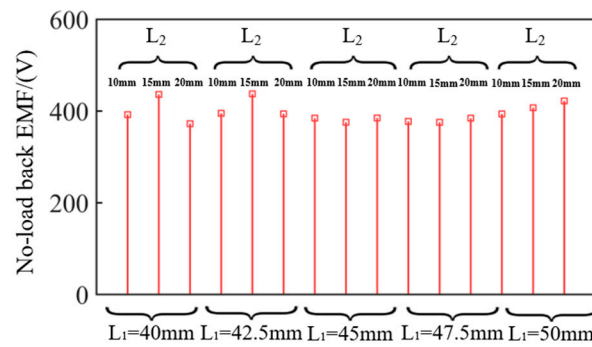
Figure 8. Analysis of the influence of the pole claw sloping shoulder distance and ring magnetic bridge length on the no−load back electromotive force amplitude.

As shown in Figure 7, the average motor torque is less affected by changes in L_1 and reaches a peak value of 6.6591 N·m when L_1 = 50 mm and L_2 = 10 mm. The torque ripple is minimal at L_1 = 42.5 mm and reaches its minimum value when both L_1 = 42.5 mm and L_2 = 10 mm, which amounts to 2.8165%. The no−load back electromotive force amplitude is observed to be larger in Figure 8 when L_1 = 40 and 45 mm, with a peak value of 437.5138 V achieved at L_1 = 42.5 mm and L_2 = 15 mm. The amplitude of the no−load back electromotive force gradually increases as the length of L_2 increases, given that L_1 is 50 mm. The observation from Figure 6 reveals that keeping L_1 constant and reducing the pole claw shoulder distance L_2 leads to a decrease in torque. As L_2 becomes shorter, an increase in the ratio of L_1/L_2 results in a larger electromagnetic torque for the motor. Conversely, when L_2 is shortened while maintaining L_1 unchanged, the electromagnetic torque decreases. This can be attributed to a reduction in the axial magnetic circuit reluctance caused by the decreased pole claw slant shoulder distance. Equations (7) and (12) demonstrate that this reduction intensifies the main air gap magnetic flux, thereby enhancing average torque.

3.3. The Influence of Semicircular Auxiliary Grooves on the Surface of Pole Claws on Average Torque, Torque Ripple, and No-Load Back Electromotive Force

The electromotive force and current waveforms of the motor will be distorted, resulting in pulsating electromagnetic torque in practical engineering applications. The auxiliary groove serves the purpose of increasing the number of fundamental wave cycles in the cogging torque, suppressing the original cogging torque, reducing the overall cogging torque, and enlarging the equivalent air gap. This contributes to a reduction in the cogging torque and minimizes the torque ripple. The traditional surface-mounted permanent magnet synchronous motor, for instance, typically incorporates a rotor auxiliary slot on its rotor surface. The RMS-HESM employs a placement of the magnetic bridge on the permanent magnet, which is positioned closer to the air gap than the outer surface of the rotor. Consequently, the permanent magnets are affixed onto the surface of the pole claws in order to achieve this configuration. In order to mitigate torque pulsation, parametric design and finite element simulation analysis were conducted on both the position and radius of the auxiliary groove. The schematic diagram in Figure 9 illustrates the position angle and radius of the auxiliary groove, where R_{slot} denotes the auxiliary radius and θ represents its position. The design range for the position angle is between 3° to 12° with a step size of 3°, while the radius of the auxiliary groove ranges from 0.5 mm to 1.5 mm with a step size of 0.5 mm.

The optimization results of R_{slot} and θ changes are shown in Table 7. The symmetrical semicircular auxiliary groove structure on the pole claw, as depicted in Figure 10, exhibits limited influence on the motor output torque while significantly impacting the torque ripple. The torque ripple is reduced at the position angles of 6° and 12° under varying auxiliary groove radii. When R_{slot} is 1 mm and θ = 12°, it reaches a minimum value of 1.8%.
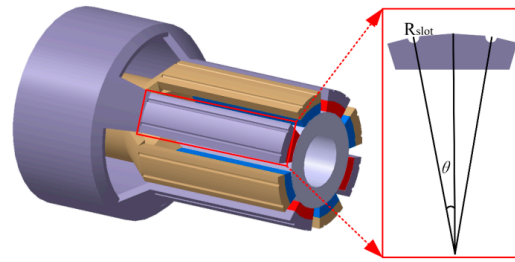
Figure 9. Schematic diagram of the position angle and radius of the auxiliary groove.

Table 7. The optimization results of R_{slot} and θ changes.

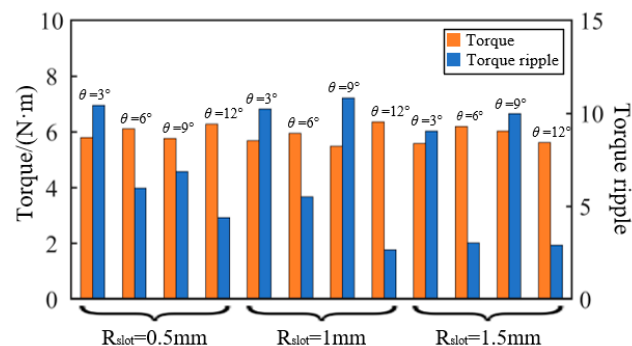| R_{slot}	θ	3°	6°	9°	12°
0.5 mm	Torque/(N·m)	5.7974	6.1089	5.7733	6.2758
	Torque ripple	10.4242	5.9763	6.877	4.3876
	EMF/(V)	420.18	382.18	388.8	424.24
1 mm	Torque/(N·m)	5.6828	5.9452	5.4921	6.3640
	Torque ripple	10.2397	5.5065	10.83	2.6666
	EMF/(V)	386.51	404.52	402.73	398.41
1.5 mm	Torque/(N·m)	5.5832	6.1931	6.0393	5.6174
	Torque ripple	9.0422	3.0386	9.9881	2.9102
	EMF/(V)	391.11	376.42	394.32	419.15

Figure 10. Analysis of the impact of the auxiliary slot position angle and radius on the average torque and torque ripple.

The amplitude of the no−load back electromotive force, as depicted in Figure 11, exhibits an initial increase followed by a subsequent decrease with respect to the radius of the auxiliary slot when R_{slot} is 1 mm. Conversely, for the R_{slot} values of 0.5 mm and 1.5 mm, there is an initial decrease in the amplitude which then transitions into an increase as the radius of the auxiliary slot increases. When the auxiliary slot radius is 1 mm, the amplitude of the no−load back electromotive force initially increases and then decreases. The minimum value of the no-load back electromotive force occurs when R_{slot} is 1 mm and $\theta = 6°$, measuring 377.8 V. Conversely, the maximum value of the no−load back electromotive force occurs when R_{slot} is 0.5 mm and $\theta = 12°$, measuring at 424.7 V.
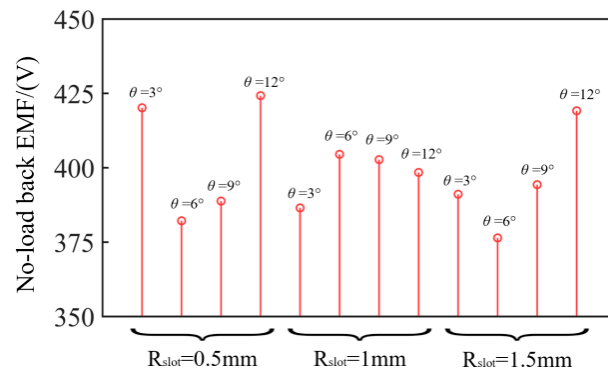
Figure 11. Analysis of the impact of the auxiliary slot position angle and radius on the no−load back electromotive force amplitude.

4. Multi-Objective Optimization Analysis of Magnetic Permeability Structure Based on PSO

The above demonstrates that by optimizing the structural parameters of the pole claws to elevate magnetic permeability, it is possible to improve the no−load back electromotive force of the motor while effectively suppressing torque pulse without compromising the output torque. The process of optimizing a single structural parameter through parametric scanning is inefficient, and it leads to the occurrence of extreme values that exhibit monotonic increases during the optimization process, thereby posing challenges for achieving convergence in the optimization results. The paper proposes a multi-objective joint simulation optimization method based on PSO, utilizing the joint simulation tools of Maxwell and Workbench and Optislong. The joint simulation model is illustrated in Figure 12 and comprises three modules: the finite element simulation module, optimization parameter set, and PSO module part. The optimization variables include the pole claw thickness, permanent magnet thickness, pole claw sloping shoulder distance, annular magnetic bridge length, and auxiliary grooves on the pole claw surface. Considering armature reaction and an excitation current of 1.5 A, the average torque, torque ripple, and no−load back EMF are designated as the objectives for optimization. The initial value and variation range of the optimization parameters should be set as indicated in Table 8 when the size is reasonable.
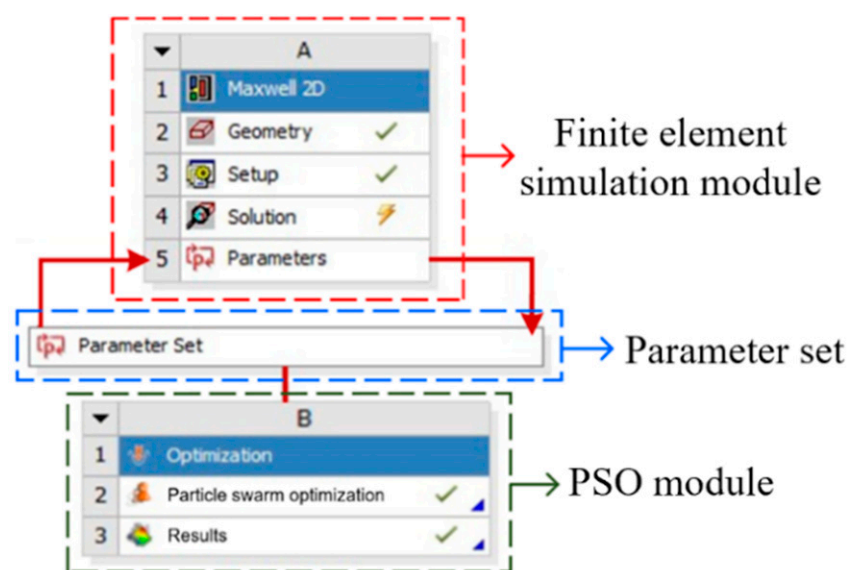
**Figure 12.** The collaborative simulation models.

Table 8. Parameter optimization range.

Parameter	Initial Value	Optimization Scope
C_{thick}/mm	6	[6, 8]
P_{thick}/mm	5.75	[6, 8]
L_1/mm	55	[40, 50]
L_2/mm	20	[10, 20]
R_{slot}/mm	0	[0.5, 1.5]
θ/°	0	[3, 12]

4.1. The Sensitivity Analysis of Optimization Parameters for Magnetic Structures and the Multi-Objective Optimization of Motors Based on PSO Is Being Studied

The aforementioned six pole claw sizes and magnetic permeability structure parameters were chosen for parameter sensitivity analysis to investigate the extent to which the optimization variables impact the optimization target.

The impact of the pole claw thickness and auxiliary slot angle on the motor output torque is evident in Figure 13, whereas the no−load back electromotive force is primarily influenced by the pole claw shoulder distance and auxiliary slot angle. It should be noted that these variables also play a crucial role in limiting the torque ripple.
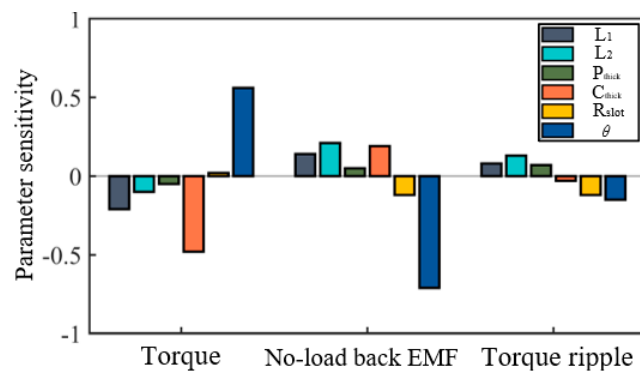
Figure 13. Parameter sensitivity analysis.

The PSO was employed for joint simulation optimization. The initial population size was set to 20, the maximum optimized population size was 2100, the maximum number of iterations was limited to 20, and a mutation rate of 30% was applied. The optimization objective function and constraints were defined according to the Equationprovided.

$$f(x) = \left[\max(EMF), \min\left(T_{\text{rip}}\right), \max\left(T_{\text{avg}}\right)\right]$$

The optimization results are presented in the form of a Pareto chart, as illustrated in Figure 14. The Pareto chart depicts the optimal solution set formed in space by the calculated optimal solutions and is represented by a three-dimensional surface connected by red dots.

The optimal solution set obtained from the optimization results on the Pareto surface depicted in Figure 14 is presented in Table 9. As can be seen from Table 9, the 19th item after optimization was selected as the optimization result. The comparison of the structural parameters before and after optimization is shown in Table 10. After the optimization, the average torque and no−load back electromotive force are 7.06 N·m and 420 V, respectively, representing an increase of 0.49 N·m and 40.44 V compared to before the optimization. Additionally, the torque ripple is reduced to 1.73%. Furthermore, through optimization, the size of the magnetic conductive part of the motor has been decreased, resulting in a reduction in overall motor size.
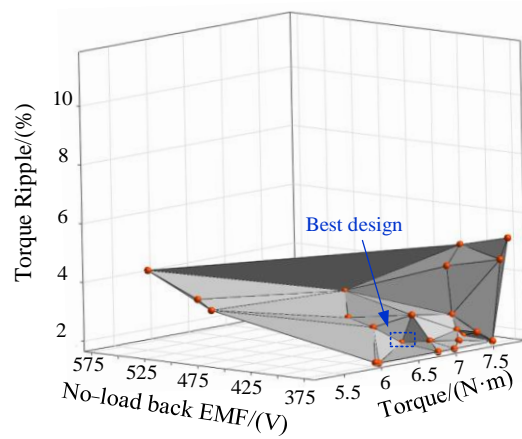
Figure 14. Pareto frontier diagram of the motor.

Table 9. Pareto optimal solution set.

Serial Number	No−Load Back EMF/(V)	Average Torque/(N·m)	Torque Ripple/(%)
1	380.2	6.57	2.91
2	534.89	5.96	3.22
3	428.51	6.79	2.34
4	581.8	5.97	3.99
5	520.86	5.94	2.91
6	379.88	6.13	1.68
7	378.49	6.94	1.67
8	377.97	7.16	1.67
9	398.45	7.48	2.07
10	464.17	6.97	2.44
11	380.5	7.93	5.07
12	415.25	7.12	2.67
13	394.18	7.51	1.89
14	382.03	7.52	2.06
15	381.88	7.27	1.88
16	497.83	7.4	3
17	376.83	7.65	1.71
18	409.41	7.58	2.49
19 (best design)	420.66	7.06	1.73
20	383.35	7.87	4.35
21	396.66	7.1	1.89
22	424.3	7.92	4.65
23	379.4	6.17	1.65

Table 10. Comparison before and after structural parameter optimization.

Motor Parameters	Initial Value	After Optimization
C_{thick}/mm	6	6.04
P_{thick}/mm	5.75	7.8
L_1/mm	50	40.95
L_2/mm	20	11.49
R_{slot}/mm	0	0.98
θ/°	0	11.77

4.2. Comparative Analysis of Multi-Objective Optimization Effects

The comparative analysis of motor torque and torque pulsation before and after optimization was conducted. The torque and pulsation values before and after optimization are shown in Figure 15. Compared with before the optimization, the average output torque

has increased significantly, from 6.57 N·m to 7.06 N·m, an increase of 7.45%. At the same time, the torque pulsation has been significantly suppressed, from 2.91% to 1.73%. Figures 16 and 17 illustrate the no−load back electromotive force and air gap flux density before and after the optimization. It can be observed that the optimized air gap flux density waveform closely resembles a sine wave, while the peak value of the motor's no−load back electromotive force exhibits a significant increase.
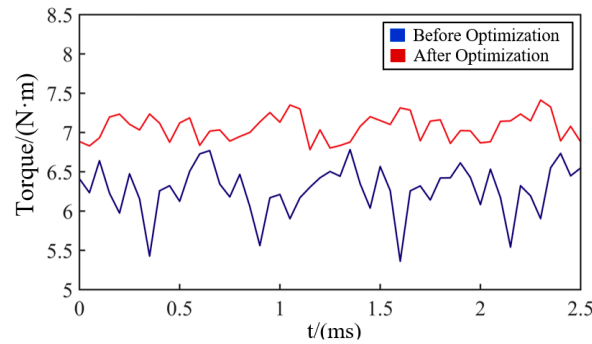

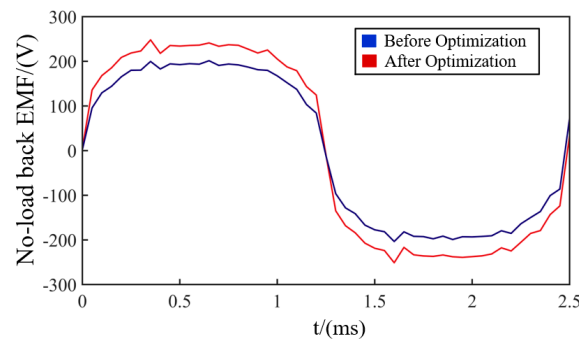**Figure 15.** Comparison before and after torque optimization.

Figure 16. Comparison before and after no − load back EMF optimization.
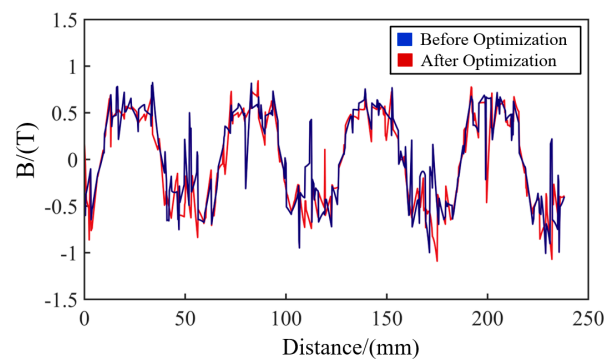

Figure 17. Comparison before and after air gap magnetic density optimization.

5. Conclusions

The focus of this paper is an RMS-HESM in marine applications, for which we establish an electromagnetic torque model and explore the influence of its unique magnetic bridge structure variation on the average torque output, torque ripple, and no−load back electromotive force of the marine motor. The Maxwell and Workbench and Optislong joint simulation tools were utilized to perform a multi-objective optimization analysis on the aforementioned structure, based on which the impact of various structural parameters on the optimization objectives was examined through parameter sensitivity analysis. Ultimately, the optimal outcome was determined utilizing a Pareto chart. The output

torque, torque ripple, and no−load back electromotive force were compared before and after optimization using a finite element simulation. The effectiveness of the optimization method was verified by comparing the waveform distribution of air gap magnetic density under no−load conditions. Consequently, the following conclusion was obtained:

The final optimization results can be obtained through joint simulation. Under rated load conditions, the average output torque is increased from 6.57 N·m to 7.06 N·m compared with before the optimization, representing a significant improvement of 7.45%. Simultaneously, there is a notable reduction in the torque ripple inhibition, which decreases from 2.91% to 1.73%.

From the sensitivity analysis, it is evident that the thickness of the pole claws and the angle of the auxiliary slot exert a significant influence on the motor's output torque. The torque ripple is primarily affected by the sloping shoulder distance of the pole claws and the angle of the auxiliary slot. Moreover, the no−load back electromotive force has a substantial impact. By strategically determining both the position and angle of the auxiliary slot at the magnetic bridge, the effective suppression of the torque ripple can be achieved while simultaneously enhancing the average torque and reducing the no−load back electromotive force.

The multi-objective optimization method effectively reduces the marine motor torque ripple and increases the no−load back electromotive force without compromising the average torque, thereby enhancing the motor air gap magnetic density and achieving a global optimization effect to improve overall ship performance.

Author Contributions: Q.Y.: writing—original draft, reviewing, project administration, and supervision; W.Z.: writing—original draft, reviewing, and validation; C.Z.: conceptualization and supervision. All authors have read and agreed to the published version of the manuscript.

Data Availability Statement: Data are available upon request from the authors.

Conflicts of Interest: The authors declare no conflicts of interest.

References

1. Husain, I.; Ozpineci, B.; Islam, S.; Gurpinar, E.; Su, G.-J.; Yu, W.; Chowdhury, S.; Xue, L.; Rahman, D.; Sahu, R. Electric drive technology trends, challenges, and opportunities for future electric vehicles. *Proc. IEEE* **2021**, *109*, 1039–1059. [CrossRef]
2. Hijikata, H.; Sakai, Y.; Akatsu, K.; Miyama, Y.; Arita, H.; Daikoku, A. Wide Speed Range Operation by Low-Voltage Inverter-Fed MATRIX Motor for Automobile Traction Motor. *IEEE Trans. Power Electron.* **2018**, *33*, 6887–6896. [CrossRef]
3. Lee, W.; Li, S.; Han, D.; Sarlioglu, B.; Minav, T.A.; Pietola, M. A Review of Integrated Motor Drive and Wide-Bandgap Power Electronics for High-Performance Electro-Hydrostatic Actuators. *IEEE Trans. Transp. Electrif.* **2018**, *4*, 684–693. [CrossRef]
4. Seo, S.-W.; Shin, K.-H.; Koo, M.-M.; Hong, K.; Yoon, I.-J.; Choi, J.-Y. Experimentally Verifying the Generation Characteristics of a Double-Sided Linear Permanent Magnet Synchronous Generator for Ocean Wave Energy Conversion. *IEEE Trans. Appl. Supercond.* **2020**, *30*, 1–4. [CrossRef]
5. Cha, J.; Yoon, J.; Bong, U.; Hahn, S. A Design Study on HTS Halbach Array for Field Coil of 40 MW Ship Propulsion Motor. *IEEE Trans. Appl. Supercond.* **2023**, *33*, 1–5. [CrossRef]
6. Liu, J.; Wang, Z.; Zhang, L. Integrated Vehicle-Following Control for Four-Wheel-Independent-Drive Electric Vehicles Against Non-Ideal V2X Communication. *IEEE Trans. Veh. Technol.* **2022**, *71*, 3648–3659. [CrossRef]
7. Zhang, Z.; Yan, Y.; Yang, S.; Bo, Z. Principle of operation and feature investigation of a new topology of hybrid excitation synchronous machine. *IEEE Trans. Magn.* **2008**, *44*, 2174–2183. [CrossRef]
8. Ahumada, C.; Tarisciotti, L.; Sepúlveda, D.; Sáez, D. Model Predictive Control for the Reduction of Marine Propellers Vibrations. In Proceedings of the 2022 IEEE Energy Conversion Congress and Exposition (ECCE), Detroit, MI, USA, 9–13 October 2022; pp. 1–8.
9. Zhang, Z.R.; Wang, D.; Hua, W. A review and outlook on the structural principles, design and operation control technology of hybrid excitation motors. *Chin. J. Electr. Eng.* **2020**, *40*, 7834–7850+8221.
10. Contò, C.; Bianchi, N. A Hybrid-Excitation Synchronous Motor with a Change in Polarity. *Machines* **2022**, *10*, 869. [CrossRef]
11. Li, J.; Wang, K. A parallel hybrid excited machine using consequent pole rotor and AC field winding. *IEEE Trans. Magn.* **2019**, *55*, 1–5. [CrossRef]
12. Mörée, G.; Leijon, M. Overview of Hybrid Excitation in Electrical Machines. *Energies* **2022**, *15*, 7254. [CrossRef]
13. Gaussens, B.; Hoang, E.; Lécrivain, M.; Manfe, P.; Gabsi, M. A Hybrid-excited flux-switching machines for high-speed DC-alternator applications. *IEEE Trans. Ind. Electron.* **2014**, *61*, 2976–2989. [CrossRef]

14. Afinowi, I.A.A.; Zhu, Z.Q.; Guan, Y.; Mipo, J.C.; Farah, P. Hybrid-excited doubly salient synchronous machine with permanent magnets between adjacent salient stator poles. *IEEE Trans. Magn.* **2015**, *51*, 1–9. [CrossRef]

15. Zhu, Z.Q.; Cai, S. Hybrid excited permanent magnet machines for electric and hybrid electric vehicles. *CES Trans. Electr. Mach. Syst.* **2019**, *3*, 233–247. [CrossRef]

16. Wu, S.; Wang, Y.; Tong, W. Design and Analysis of New Modular Stator Hybrid Excitation Synchronous Motor. *CES Trans. Electr. Mach. Syst.* **2022**, *6*, 188–194. [CrossRef]

17. Chen, Y.; Zhou, X.; Li, Z.; Zhu, X. Torque Performance Enhancement for Hybrid PM Motor Considering Magnet Characteristic Difference and Variation. *IEEE Trans. Magn.* **2023**, *59*, 1–5.

18. Yang, Q.; Pang, L.; Shen, H.; Qin, H.; Zhao, C. Influence of excitation current on electromagnetic vibration and noise of rotor magnetic shunt hybrid excitation synchronous motor. *Energy Rep.* **2022**, *8*, 476–485. [CrossRef]

19. Wang, C.; Zhang, Z.R.; Liu, Y. Rotor eddy current loss and heat dissipation optimization of high torque density rotor magnetic shunt hybrid excitation motor. *Chin. J. Electr. Eng.* **2021**, *41*, 7476–7486.

20. Pierpaolo, D.; Saponara, S. Control System Design for Cogging Torque Reduction Based on Sensor-Less Architecture. In *Applications in Electronics Pervading Industry, Environment and Society. ApplePies 2019*; Saponara, S., De Gloria, A., Eds.; Lecture Notes in Electrical Engineering; Springer: Cham, Switzerland, 2020; Volume 627.

21. Bernardeschi, C.; Dini, P.; Domenici, A.; Saponara, S. Co-simulation and Verification of a Non-linear Control System for Cogging Torque Reduction in Brushless Motors. In *Software Engineering and Formal Methods, Proceedings of the SEFM 2019, Oslo, Norway, 16–19 September 2019*; Camara, J., Steffen, M., Eds.; Lecture Notes in Computer Science; Springer: Cham, Switzerland, 2020; Volume 12226.

22. Dini, P.; Saponara, S. Model-Based Design of an Improved Electric Drive Controller for High-Precision Applications Based on Feedback Linearization Technique. *Electronics* **2021**, *10*, 2954. [CrossRef]

23. Jiang, J.W.; Bilgin, B.; Yang, Y.; Sathyan, A.; Dadkhah, H.; Emadi, A. Rotor skew pattern design and optimisation for cogging torque reduction. *IET Electr. Syst. Transp.* **2016**, *6*, 126–135. [CrossRef]

24. Lee, S.-G.; Kim, S.; Park, J.-C.; Park, M.-R.; Lee, T.H.; Lim, M.-S. Robust Design Optimization of SPMSM for Robotic Actuator Considering Assembly Imperfection of Segmented Stator Core. *IEEE Trans. Energy Convers.* **2020**, *35*, 2076–2085. [CrossRef]

25. Ou, H.; Hu, Y.; Mao, Z.; Li, Y. A Method for Reducing Cogging Torque of Integrated Propulsion Motor. *J. Mar. Sci. Eng.* **2019**, *7*, 236. [CrossRef]

26. Kanapara, A.J.; Badgujar, K.P. Performance Improvement of Permanent Magnet Brushless DC Motor through Cogging Torque Reduction Techniques. In Proceedings of the 2020 21st National Power Systems Conference (NPSC), Gandhinagar, India, 17–19 December 2020; pp. 1–6.

27. Wang, C.; Zhang, X.; Wang, P. Cogging torque optimization of double-layer interior permanent magnet synchronous motor. *China Sci. Pap.* **2021**, *16*, 906–910.

28. Zou, D.; Cao, J. Effect of stepped rotor on cogging torque of double stator flux reversal machine. *Small Spec. Electr. Mach.* **2021**, *49*, 11–16.

29. Sun, Y.; Fang, Y.; Zhang, Q.; Liu, Q. Optimal Design of Marine Motors for Joint Efficiency and Economic Optimization. *Energies* **2023**, *16*, 4588. [CrossRef]

30. Zheng, S.; Zhu, X.; Xu, L.; Xiang, Z.; Quan, L.; Yu, B. Multi-objective optimization design of a multi-permanent-magnet motor considering mag-net characteristic variation effects. *IEEE Trans. Ind. Electron.* **2022**, *69*, 3428–3438. [CrossRef]

31. Fan, D.; Quan, L.; Zhu, X.; Xiang, Z.; Que, H. Airgap-harmonic-based multilevel design and optimization of a double-stator flux-modulated permanent-magnet motor. *IEEE Trans. Ind. Electron.* **2021**, *68*, 10534–10545. [CrossRef]